DOI: ADD DOINUMBER HERE

Aerothermal analysis of plume interaction with deployed landing legs of the CALLISTO vehicle

Moritz Ertl[⋆]*, Tobias Ecker*[⋆]*, Josef Klevanski*[⋆]*, Etienne Dumont*[†] *and Sven Krummen*[†]
German Aerospace Center (DLR)
[⋆] *Institute of Aerodynamics and Flow Technology*
Bunsenstr. 10, 37073 Goettingen, Germany
[†] *Institute of Space Systems*
Robert-Hooke-Str. 7, 28359 Bremen, Germany
moritz.ertl@dlr.de · tobias.ecker@dlr.de · josef.klevanski@dlr.de
etienne.dumont@dlr.de · sven.krummen@dlr.de

Abstract

The current European long term strategy [1] aims at moving towards reusable launch vehicles (RLV) for the first stages of launchers. In accordance with this strategy the German Aerospace Center (DLR) has entered into a collaboration with the Japan Aerospace Exploration Agency (JAXA) and the French Space Agency (CNES) for the development of RLV relevant technologies. A part of this collaboration is a vertical take-off and vertical landing (VTVL) reusable subscale launcher first stage demonstrator - the "Cooperative Action Leading to Launcher Innovation in Stage Toss back Operations" (CALLISTO) [2, 3]. The mission of the CALLISTO vehicle is to return to the launch pad using retro propulsion and an Approach and Landing System (ALS) [4] with extendable landing legs. This development leads to additional aerothermal design questions compared to traditional launchers. In the case of CALLISTO the highest heat fluxes are caused by heating from hot exhaust gases of the aft bay section. This especially affects the unfolded ALS during the final phase of the landing approach. The arising heat fluxes, therefore, influence the structural design and the thermal protection system (TPS) of the ALS. In this study we conduct computational fluid dynamics (CFD) investigations using Reynolds averaged Navier Stokes (RANS) methods of the aerothermal loads on the ALS during the landing phase. We use the Spalart-Allmaras turbulence model and frozen chemistry for the simulations. We analyse the flow field as well as the surface distributions. We investigate the necessity of simulations including the plume for these analyses. We use analyses of the flow fields as well as the surface distributions to investigate the influence of angle of attack, angle of roll, atmospheric conditions, flight speed and thrust level.

1. Introduction

Space launches are expensive. One of the reasons is that, conventional launch vehicles are only single use. Therefore, one way of reducing the cost of launches is to reuse expensive parts of the vehicle, as has been demonstrated by SpaceX with the first stage of Falcon 9 [5]. Europe and Japan, while they are finalising the development efforts for their new conventional launcher generations, have started the research and development on reusable launch vehicles in a cooperation. The "Cooperative Action Leading to Launcher Innovation in Stage Toss back Operations" (Callisto) [2] vehicle is a flight demonstrator for future reusable launcher stages and their technologies. The program involves three countries and their space organizations: CNES for France, DLR for Germany and JAXA for Japan. The first tests will be conducted in 2024 from CSG, Europe's Spaceport. The challenge is to develop, all along the project, the skills of the partners. This know-how includes products and vehicle design, ground segment set up, and post-flight operations for vehicle recovery then reuse.

Callisto is a first stage demonstrator for vertical take-off and vertical landing (VTVL) with a single liquid hydrogen-oxygen engine. Its mission is to vertically launch and return the single stage vehicle to the launch pad. For the return flight the demonstrator first employs a phase of glide, during which the drag is used to break the vehicle, followed by the re-ignition of the engine and and retro-propulsion breaking before utilising its Approach and Landing System (ALS) [4, 6] with extendable legs to land on the pad. One of the big differences between a vertical landing reusable launcher and a conventional launcher is the retro-propulsion phase. During this phase the plume is directed towards the direction of flight and against the air flow. Thus, the hot exhaust gases are are pushed back onto the vehicle

structure and especially the landing legs in their deployed state. The interaction of the hot exhaust plume with the vehicle causes additional heat fluxes onto the structures, which in our case of subsonic retro-propulsion can constitute the bulk of the critical heat loads. Despite the existence of industrial projects on VTVL reusable rockets there are not many published studies on the topic in general or on the aerothermodynamics specifically. Ecker et al. [7] investigated the thermal loads on Falcon 9. Ecker also did an analysis for Callisto during an earlier design phase on a preliminary, simpler geometry without considering deployed landing legs in Dumont et al. [8]. Laureti and Karl [9] created an aerothermal database and investigated the heat fluxes for the EU Horizons 2020 project Retro propulsion Assisted Landing Technologies (Retalt). They based their research on a 3D vehicle with nine engines, modeled after the Falcon 9 rocket, and focused their investigation on base plate and fin heat loads, but did not present results for a configuration with deployed landing legs.

Since a study of the aerothermal loads in the configuration with deployed landing legs is necessary for a vertical landing reusable launcher - both for the overall design of the vehicle and the subsystems - and since the literature on this topic so far is sparse, we aim to provide an overview of the analyses and investigation we undertook in order to provide a aerothermal database. We describe the methodology used for the creation of the ATD and we present selected results to illustrate the influence of different flight and operation parameters on the heat loads.

2. Methodology for the database creation

The aerothermal database (ATD) for the Callisto vehicle has been created for different vehicle configurations and trajectory points. In this paper we limit ourselves to the configuration with deployed landing legs, called the UUO configuration (unfolded fins, unfolded legs, engine on). This is the only relevant configuration for this investigation, as during the approach and landing phase with deployed legs the fins will always be deployed and the engine will always be on. The deployment of the landing legs happens at an defined altitude, limiting the data point space for the ATD to the densities and velocities provided in table 1. These data points are chosen and spaced in such a way, that possible trajectory points can be interpolated from the ATD. For more information on the data point selection see Ecker et al. [10].

Table 1: Simulated points

Mach	**Density**	**AoA**
$[-]$	$\left[\mathrm{kg\,m^{-3}}\right]$	$[^\circ]$
0.5	1.1786	190, 185, 180, 175, 170
0.2355	1.2075	180, 170, 155
0.1	1.2215	180, 170, 155

The ATD is created from CFD simulations. The simulations were done using the DLR TAU code. In the next section the fundamentals of the code are introduced and the numerical setup common to all simulations is described. While Callisto also has extensive wind tunnel results for validating the aerodynamic data [11] and a good comparison can be shown [12], for the heat fluxes only CFD results exist. This is due to the fact, that wind tunnel tests with a hot exhaust plume are very difficult and expensive. As Callisto is a research project with limited funding this shortcoming has to be accepted and a comparison with heat flux sensor results will be performed after the test flights. Additionally, the Tau code is well validated [13] for these problems and some fundamental experiments for validation are currently underway.

2.1 Numerical method

The TAU code [13] is a finite volume (FV) CFD code, which is solving the Reynolds averaged Navier-Stokes (RANS) equations on hybrid structured-unstructured meshes for 2D and 3D problems. The TAU code is used with the 2. order upwinding difference scheme AUSMDV [14] for the spatial discretization and least squares reconstruction for the gradients. A modification of the variable reconstruction according to Thornber [15] is employed to improve the computation for low Mach numbers. An explicit Runge-Kutta scheme is used for the temporal discretization. A wide selection of turbulence models, from one-equation Spalart-Allmaras models, over two-equation k-ω-models, to Reynolds stress models (RSM) is available.

2.2 Numerical setup

The Callisto CAL1C configuration is complex non-symmetrical geometry with pipes and cable ducts. Thus the simulation is done with a full 3D model. The Callisto CAL1C vehicle geometry is used to non-dimensionalise the results. It has a diameter $D = 1.1$m and a length $L = 13.455\text{m} \approx 12.23D$. The computational domain is a spherical far field with a diameter of $10L$. A hybrid structured-unstructured mesh with a total of 23 million elements is used for the discretization. The entire mesh as well as some select regions is shown in figure 1.

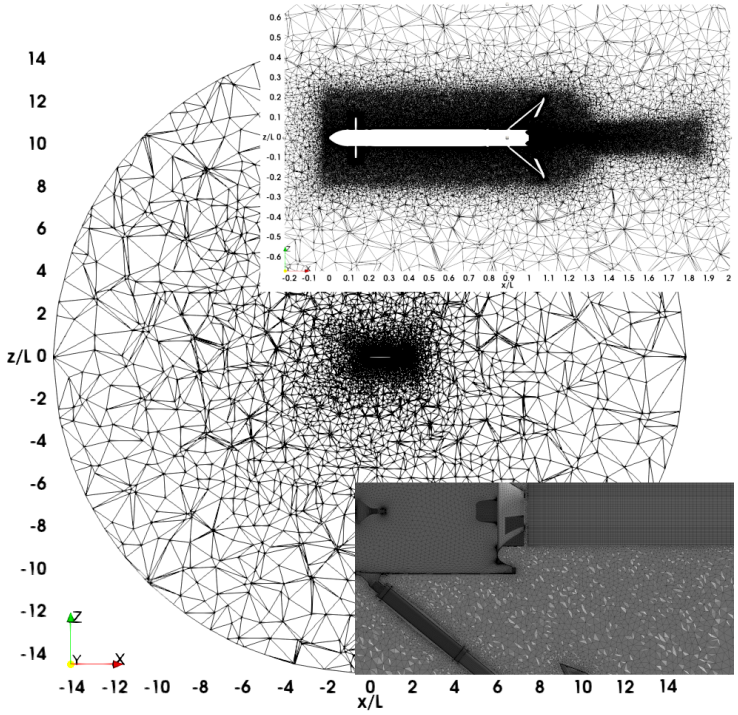

Figure 1: Computational grid for CAL1C UUO configuration with zoomed regions for local refinement and block structured region.

A grid refinement is used in the vicinity around the vehicle and in the plume region with an additional refinement around the fins. Furthermore a structured mesh section is employed for the jet core area behind the nozzle. At viscous walls 20 prism layers with a first layer size chose in such way, that for the entire vehicle a dimensionless wall distance of $y+ < 1.0$ is ensured.

The far field boundary condition and the reference are set to the trajectory values provided in table 1 and the temperature is set to $T_\infty = 300$K. The vehicle surfaces are set as viscous walls with the wall temperature $T_{wall} = T_\infty = 300$K. The nozzle is modelled as a Dirichlet boundary condition, which is obtained in a two step process. In the first step the combustion chamber conditions are calculated from the engine data with NASA CEA []. In the second step these conditions are used as boundary conditions to run a 2D simulation with the nozzle geometry and a frozen chemistry representative “exhaust gas” species, which is a single gas combination of the resulting combustion species mixture. The output from the 2D nozzle simulation is used to interpolate the velocity profile and the species distribution onto the above mentioned Dirichlet boundary condition. The main simulations are then carried out with frozen chemistry and a two gas species - air at the trajectory point conditions and the “exhaust gas” mixture. This entire procedure is utilised for the calculation of both thrust levels. Two thrust levels Th are used in this investigation: one designated $Th = 110\%$, which represents the maximum thrust and a lower thrust level $Th = 40\%$. For more information on the engine settings please refer to our other paper[10].

2.3 Zoning of the landing legs

The ATD data is post processed to be provided to the overall system and the product design teams in a useful acuity. For the heat flux, area averaged values, integral values as well as maximum and minimum values are provided instead

of the values for every single surface grid point. The heat flux will be presented as the dimensionless Nusselt number

$$Nu = \frac{qL}{k\,(T_{cc} - T_\infty)}, \tag{1}$$

where heat flux q, thermal conductivity of air k, characteristic length $L = D$ and the temperatures of the combustion chamber T_{cc} and the reference and wall temperature $T_\infty = 300\text{K} = T_w$. The integral heat flux is obtained by summing the values for all points j in a chosen zone Z and the average is done over the sum of the respective cell areas

$$Nu_{int} = \sum_Z Nu_j, \quad Nu_{av} = \frac{Nu_{int}}{\sum_Z A_j}. \tag{2}$$

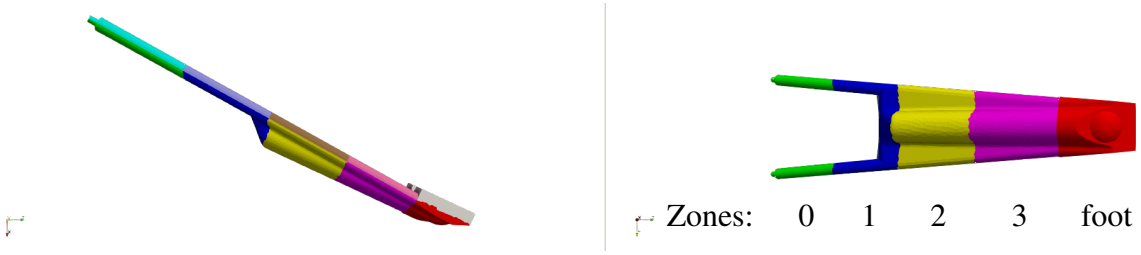

Figure 2: Refined zoning of the Callisto landing legs with 10 custom zones for higher acuity in integral and average heat flux values.

The zones were chosen in consultation with the responsible product team. The zoning for the landing legs is shown in figure 2. The legs are zoned with four radial cuts into five radial sections and then further with a plane into upper and lower sections for a total of 10 zones. The vertical zoning is labeled upper half and lower half and the radial zones are are numbered from 0 to 4 going outward from the vehicle center with the last zone being labeled “foot”. More information on the zoning procedure can be obtained from Ecker[10].

3. Results

3.1 General flow field observations

The general interactions between the engine plume and the vehicle structure during reverse flight are shown in figure 3, for the case of Mach number $Ma = 0.5$, a density $\rho = 1.18\text{kg m}^{-3}$ and an angle of attack $AoA = 170°$. The direction of the flow is from bottom to top.

On the left the Mach number distribution is exhibited on a x-z slice through the centre line of the vehicle with added stream lines. The vehicle and plume interact with the reverse flow from the backward flight. While the under expanded plume core is symmetric, exhibiting a classical shock pattern, the outer parts of the plume are deformed in the direction of the flow and get pushed onto the vehicle structure and the landing legs. The stream lines show part of the flow moving from left to right around the vehicle body due to the angle of attack.

On the right the dimensionless Temperature Θ is shown on the same slice. It is defined as

$$\Theta = \frac{(T - T_\infty)}{(T_{cc} - T_\infty)}, \tag{3}$$

with the chamber temperature $T_{cc} \approx 3500\text{K}$ and the reference temperature $T_\infty = 300\text{K}$. Additionally the dimensionless heat flux is shown on the vehicle surface as Nusselt number Nu, which has already been defined in equation 1. The temperature distribution shows, that the hot exhaust gases are transported all along the length of the vehicle along the stream lines of the air flow. This leads to parts of the vehicle, especially the right leg and the aft bay getting heated, with the highest heat fluxes observed on the struts of the landing legs and on the base plate and lowest part of the aft bay. At the same time, due to the direction of the air flow, parts of the vehicle are not exposed to the plume at all. This leads to the left landing leg only seeing positive heat fluxes at the struts close to the vehicle, while the further parts are even cooled by the air flow. The same can be observed for the fins and also leads to the leeward side of the struture seeing the higher heat fluxes.

The dimesionless heat fluxes to the landing legs are plotted in figure 4. The heat fluxes are shown for all legs and for the post processing zones introduced in section 2.3 for the lower half of the landing legs. The mean heat fluxes, provided in the first plot, are in accordance with both the flow field described in the previous section and the Nu contour

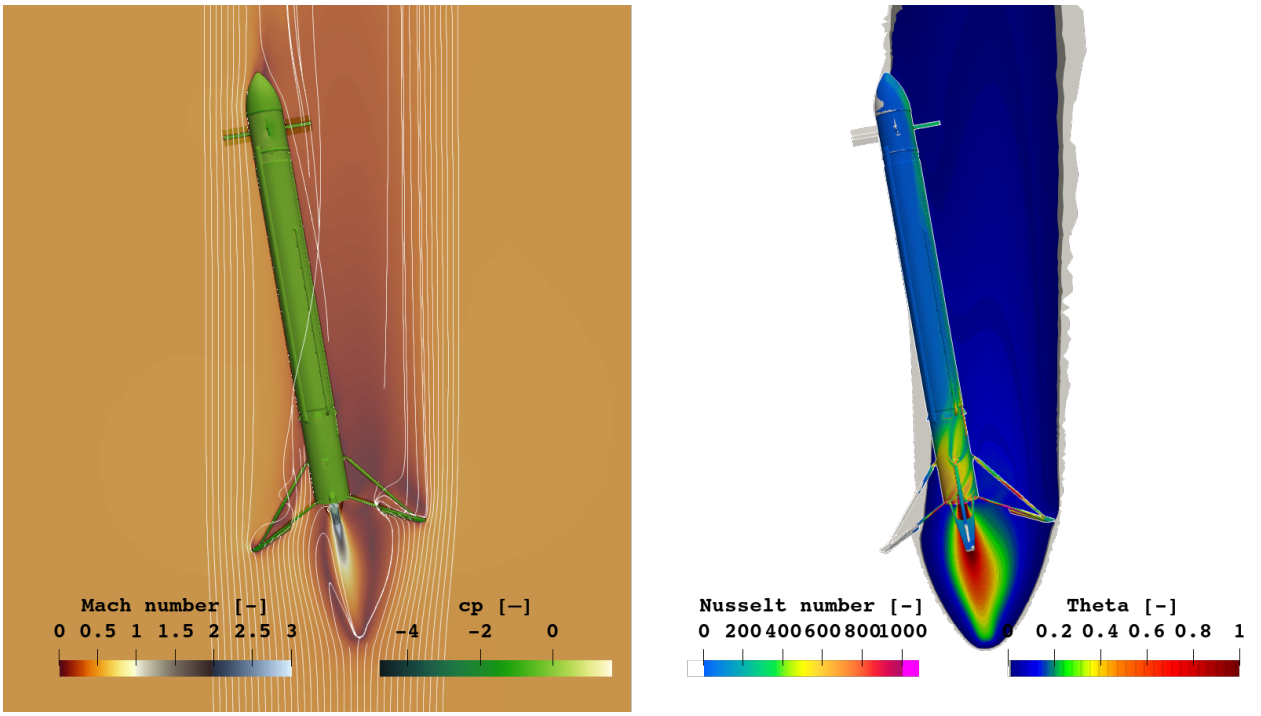

Figure 3: Flow field of Callisto UUO configuration at $Ma = 0.5$, $\rho = 1.18\text{kg}\,\text{m}^{-3}$ and $AoA = 170°$. On the left, Mach number Ma slice through the centre line with velocity stream lines and c_p on the vehicle surface. On the right, dimensionless temperature Θ slice and dimensionless heat flux Nu on the vehicle surface.

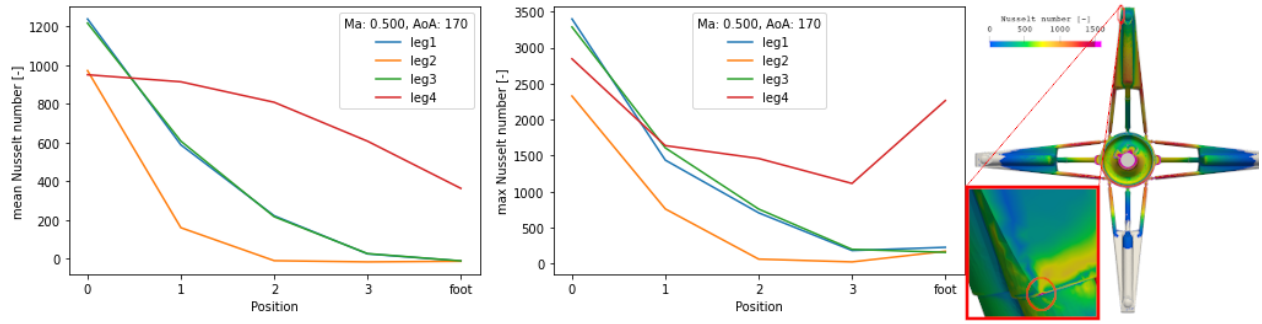

Figure 4: Plots of mean and max dimensionless heat flux Nu for differnt sections of the landing legs for $Ma = 0.5$, $\rho = 1.18\text{kg}\,\text{m}^{-3}$ and $AoA = 170°$. On the right the bottom view of the landing legs with Nu contouring and a cut out showing the heat flux peak.

at the right of figure 4. Leg 4, which is the leg on the right in figure 3, receives the highest average heat fluxes and leg 2, on the left, receives the lowest both due to the deflection of the plume. Legs 1 and 3 are receiving mean Nu in between, excep for zone 0, the section closest to the vehicle. In accordance with the Nu contoure leg 4 receives less heat flux close to the vehicle. This is most likely due to the aft bay structure deflecting part of the flow.

The second plot provides the maximum values of Nu which occure in the same zones. The maxima exceed the mean values by a factor of about two to three. The general development is similar to the mean Nu plot except for one outlier with the foot of leg 4 exhibiting a higher max Nu compared to the zones closer to the vehicle. A first look at the flow field and the heat flux contour does not confirm this development, but a closer look reveals a local spot of high heat flux at the side of the foot. These local over estimations are numerical artefacts which mainly occure near sharp edges. An approach utilising both the maximum and the mean values in combination with a fine zoning of the surfaces was therefore chosen to proived accurate information to the system and product design teams.

3.2 Influence of angle of attack

The influence of the angle of attack is shown in figure 5 for $AoA = 185° - 170°$ using the same Θ slice and Nu surface as figure 3. The case of $AoA = 180°$ (second picture) exhibits a symmetrical flow field in the stream lines as well as in the temperature field. Also the landing legs have a symmetric heat flux distribution, with highest heat fluxes around the centre of the struts. The heat flux to the vehicle is lowest for this angle of attack and rather evenly distributed along the aft bay and lower structure. The $AoA = 170°$ case (last picture) has already been discussed in the last section. The comparison with the lower angles of attack shows a strong heating of the aft bay, while the rest of the vehicle is exposed to a lower heat flux, due to the steeper angle.

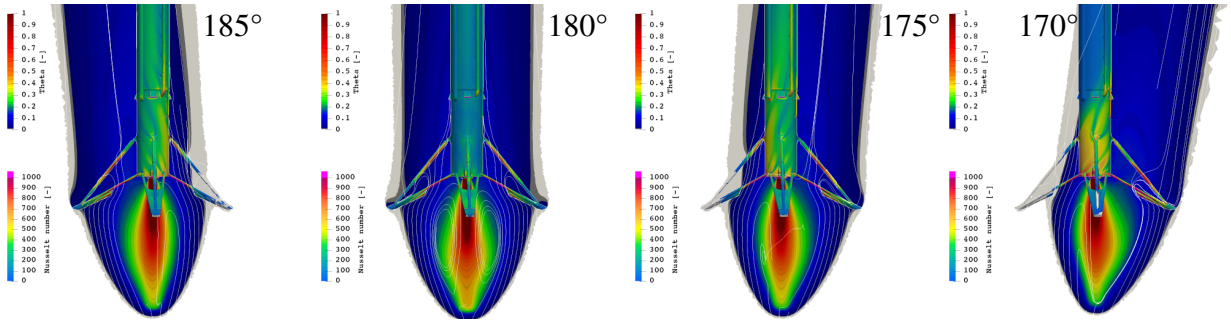

Figure 5: Influence of angle of attack. Slices through the centre line with velocity stream lines, dimensionless temperature Θ slice and dimensionless heat flux Nu on the vehicle surface for angles of attack $AoA = 185°, 180°, 175°$ and $170°$.

The cases of $AoA = 185°$ and $AoA = 175°$ (first and third picture) are analogous to the $AoA = 170°$ case, both exhibit part of one landing leg outside the exhaust plume receiving lower heat fluxes and even getting cooled from the air flow, while the opposite leg is exposed more strongly to the deflected plume, receiving higher heat fluxes. The region of highest heat flux on the struts moves outward with increased AoA. The aft bay heat flux distribution is also largely mirror-inverted, but on the centre part of the vehicle some differences can be observed, due to the flow interacting with the pipes and cable ducts.

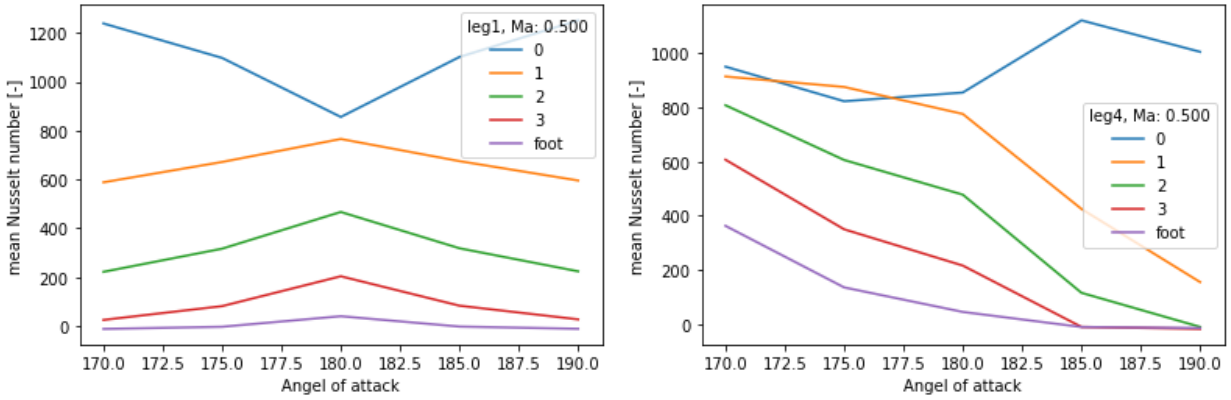

Figure 6: Plot of dimensionless heat flux Nu over angle of attack AoA for the different zones of leg 1 (left) and leg 4 (right).

The plots of mean Nu over AoA shown in figure 6 support the analysis of the flow field. The results are shown for the lower half zones of two of the landing legs. Leg 1, which is situated in the centre in figure 5 exhibits a symmetrical behaviour. The heat fluxes decrease with distance to the vehicle centre. For all zones excep zone 0 the highest heat fluxes occure for the undeflected plume $AoA = 180°$ and decreasing slightly with higher angles of attack, while for zone 0 the behviour is inverted. Leg 4, which is the leg to the right in figure 5, the heat fluxes decrease with an increased angle of attack as the leg is turning more and more out of the plume, again with an exception of zone 0. The plots for leg 2 and leg 3 are not shown, as leg 3 shows the same behaviour a leg1 and leg 2 is the mirror-inverted of leg 4.

3.3 Influence of roll angle

The influence of the roll angle *AoR* on the aerothermodynamics is demonstrated with the help of figure 7. Two roll angles are compared for the case of $Ma = 0.5$ and $AoA = 170°$, with $AoR = 0°$ on the left and $AoR = 45°$ on the right. The top row shows a side view with temperature field and *Nu* and the bottom row shows a bottom view of the landing legs with *Nu* contouring.

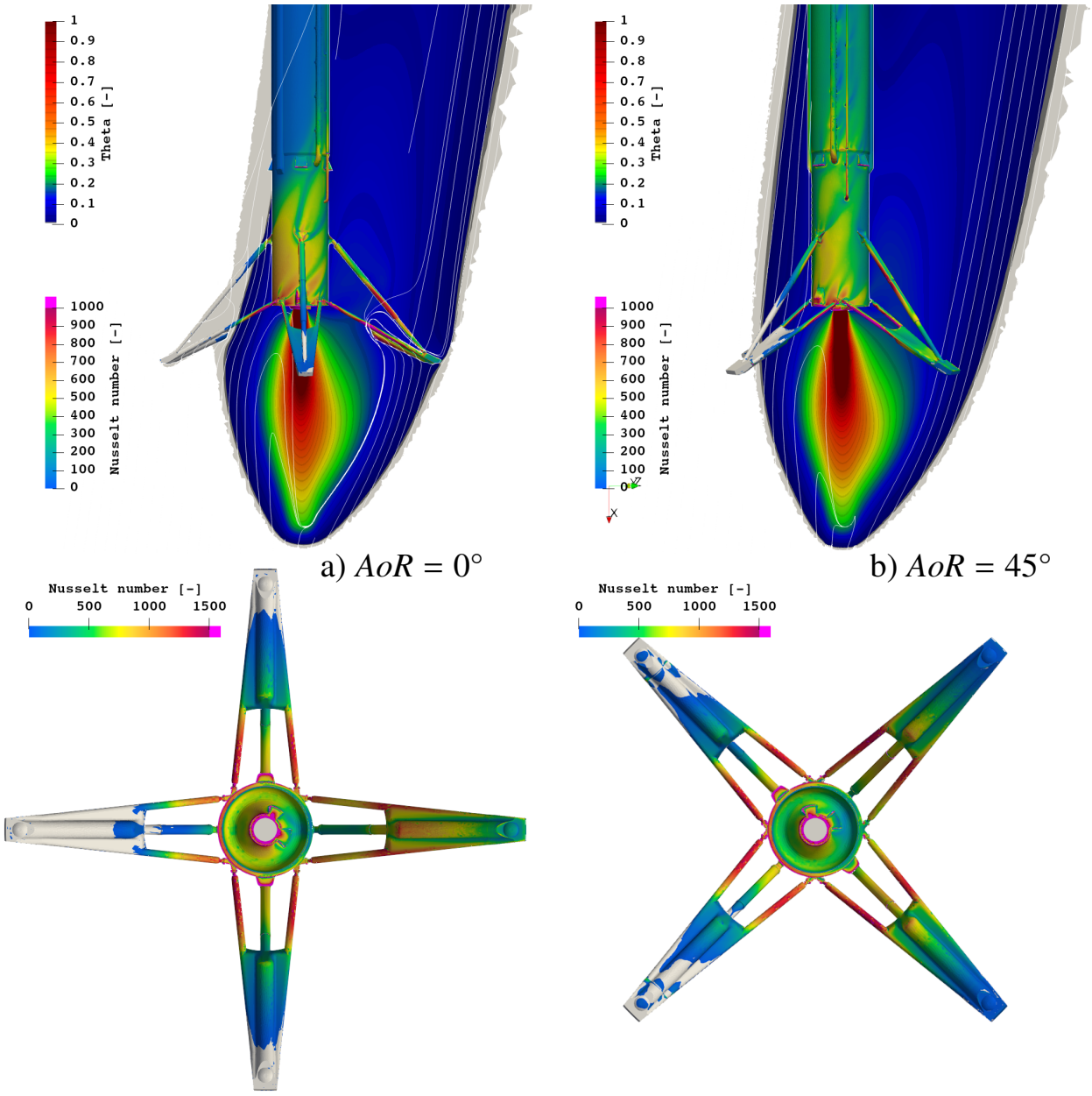

Figure 7: Influence of angle of roll. On the left a) $AoR = 0°$, on the right b) $AoR = 45°$. Top row showing slices through the centre line with velocity stream lines, dimensionless temperature Θ slice and dimensionless heat flux *Nu* on the vehicle surface for $Ma = 0.5$ and $AoA = 170°$. Bottom row showing bottom view of landing legs with *Nu*.

The visualisation shows a clear influence of the roll angle in cases of inclination $AoA \neq 180°$. For $AoR = 0°$ the plume is deflected towards the leg to the right, leading to high heat fluxes onto the entire right foot pad. The left footpad receives nearly no heat and the upper and lower feet are seeing low heat fluxes. In the case of $AoR = 45°$ the main part of the plume is passing in between the two landing legs on the right. Both foot pads on the right see medium heat fluxes, while on the left the heat fluxes are lower. For both roll angles the highest observed heat fluxes are on the lower struts.

There are also slight differences in the heat flux to the vehicle structure. For $AoR = 0°$ the relevant heat fluxes are limited to the aft bay, while the rest of the vehicle structure receives heat fluxes of $Nu < 200$. For $AoR = 45°$ on the other hand, the further topwards structures of the vehicle are also heated. This is due to the landing leg additionally deflecting the flow for $AoR = 0°$, as can be observed from the stream lines.

3.4 Influence of Mach number and engine thrust level

The influence of flight Mach number Ma and the thrust level of the engine Th were investigated. Figure 8 shows the temperature field Θ and the heat flux Nu for different Ma and Th. To better illustrate the effects the scale of the temperature has been changed to $\Theta = [0 - 0.25]$ in contrast to the previous visualisations. The density for the $Ma = 0.5$ case is $\rho = 1.1786\text{kg m}^{-3}$ and for both $Ma = 0.2355$ cases it is $\rho = 1.2075\text{kg m}^{-3}$. The densities are similar enough to be considered as having an only minor influence on the plume behaviour.

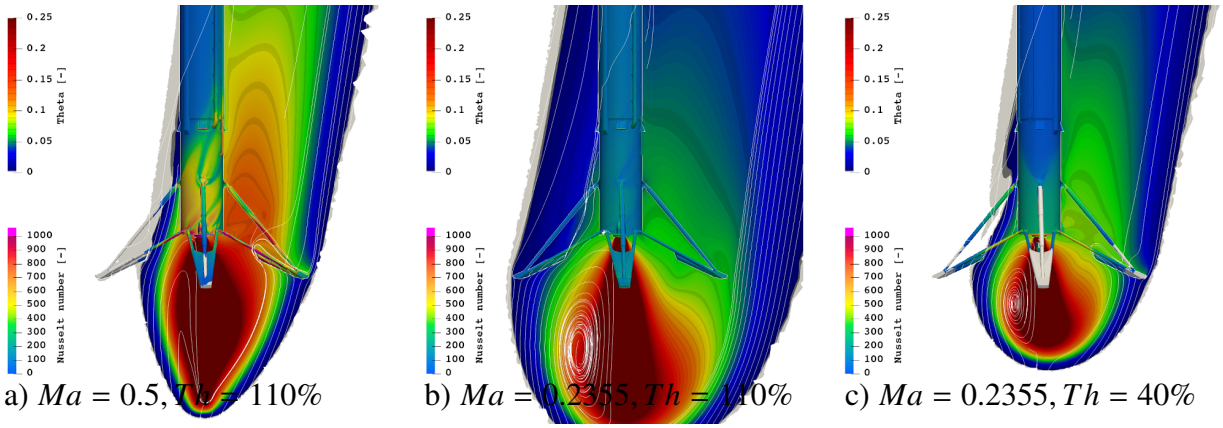

Figure 8: Influence of Mach number and thrust level. Slices through the centre line with velocity stream lines, dimensionless temperature Θ slice and dimensionless heat flux Nu on the vehicle surface for $AoA = 170°$ and for a) $Ma = 0.5, Th = 110\%$, b) $Ma = 0.2355, Th = 110\%$ and c) $Ma = 0.2355, Th = 40\%$.

The comparison of the first two visualisations illustrates the influence of different flight Mach numbers. Two big differences become apparent for the lower $Ma = 0.2355$: First, the plume is larger in radial extension, being less strongly compressed by the lower stream w ise velocity of the air flow. It encompasses the entire landing legs. Second, the temperature field shows lower temperatures around the legs and the vehicle structure, again due to lower air flow velocities. As a result the observed heat flux maxima to the vehicle and legs are a lot lower for lower Ma. However, since the entirety of all legs is now affected by the plume no regions of cooling by the air flow exist.

The comparison of the second and the third visualisation illustrates the influence of different thrust levels. For $Th = 40\%$ the plume is narrower, having a more similar extension to the $Ma = 0.5, Th = 110\%$ case, due to the lower jet velocity interacting with the lower air flow velocity. Parts of the footpads are again outside of the plume and getting cooled. The region of higher temperatures Θ is more compact, as in the $Ma = 0.2355, Th = 110\%$ case, but also closer to the vehicle structure. The resulting heat flux maxima are higher compared to the $Ma = 0.2355, Th = 110\%$. The heat flux distribution is less even, as in the $Ma = 0.5, Th = 110\%$ case, but at clearly lower levels.

3.5 Influence of turbulence model

The different approaches to modelling turbulence in RANS are one of the sources of uncertainties. To quantify this influence, four different turbulence models are investigated

- Spalart Allmaras one-equation model [16]
- Wilcox k-ω 1998 two-equation model [17]
- SST Menter 2003 two-equation model [18]
- RSM Reynolds stress model [19].

The turbulence models are listed with increasing modelling quality. The higher quality comes at the prize of increased computational cost. The influence of the different turbulence models is visualized in figure 9 with dimensionless

temperature shown as a 2D slice in the x-z-plane and the dimensionless heat flux shown as Nusselt number on the surfaces of the vehicle structure.

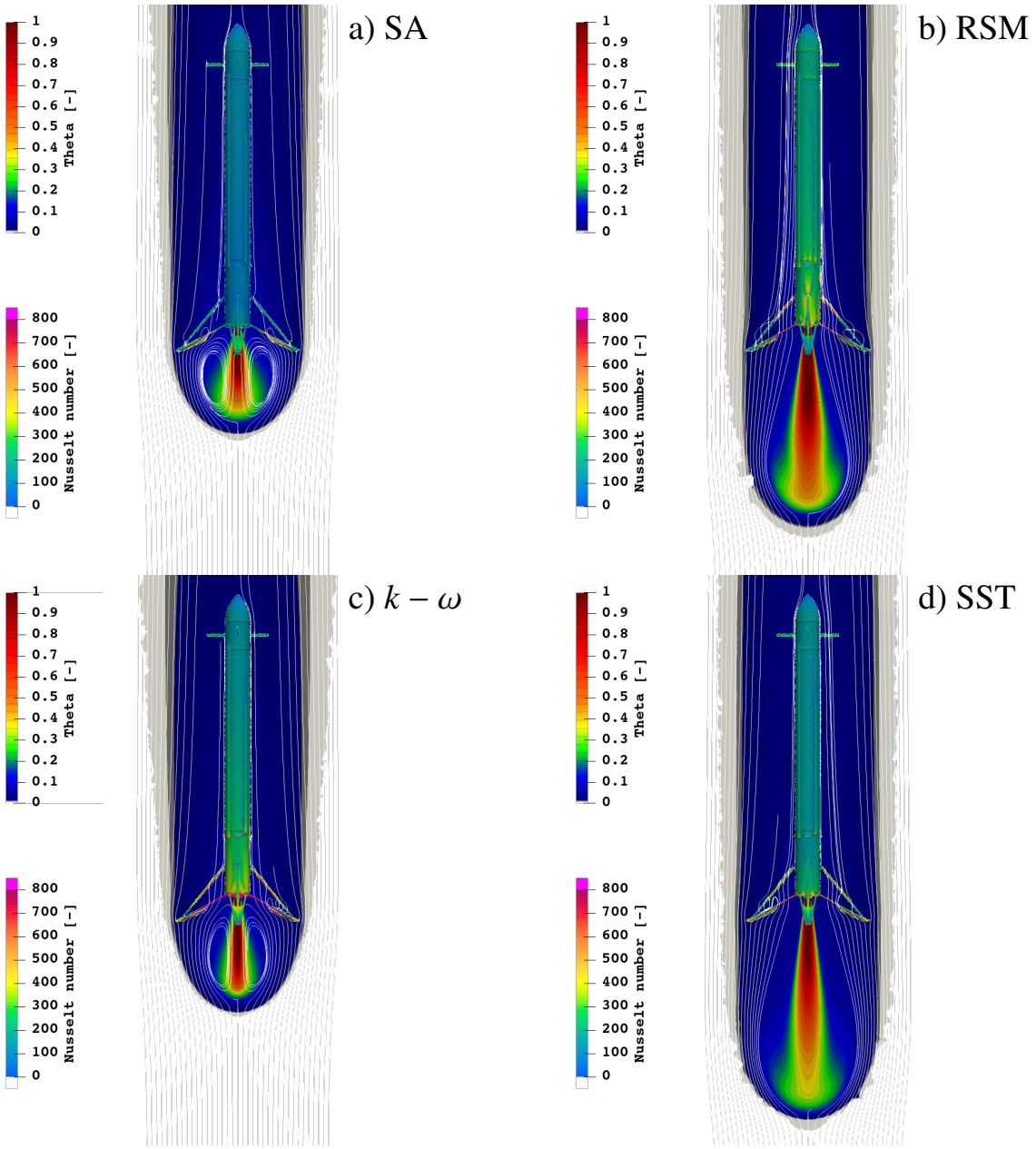

Figure 9: Comparison of four different turbulence models. Side view of a centre line slice cut of dimensionless temperature Θ and dimensionless heat flux Nu on the vehicle surface. $Ma = 0.299$, $\rho = 1.127\text{kg m}^{-3}$ and $AoA = 180°$.

The temperature field illustrates the differences between the different turbulence models. The plume cores differ strongly in both axial and radial extension. The SA and $k-\omega$ model provide a shorter axial plume, while the SST and RSM models lead to a longer axial extension. Additionally, the $k-\omega$ model shows the smallest radial extension, while a medium extension is obtained for the SA and RSM plumes and the SST model provides the largest radial extension. The SA and SST models predict only a low heat flux to the vehicle structure, seeing mainly heat flux to the landing legs and aft bay. The $k-\omega$ model predicts relevant heat fluxes to the lower half of the vehicle and the RSM model predict a heat flux of $Nu > 200$ onto most of the structure. In line with the heat flux to the structure, the heat flux to the landing legs is lowest for the SA and the SST models. However, the $k-\omega$ model shows the highest Nu maxima even exceeding the RSM simulation. These are due to the $k-\omega$ model plume being more compact and thus exhibiting higher Θ in the region of the landing legs.

The comparison of the turbulence models shows the big influence this modelling choice has on the simulation

results. In absence of experimental data on heat fluxes prior to the test flights, the results of this comparison are used to provide an uncertainty estimation for the ATD.

4. Conclusions

We presented our methodology used for the creation of an aerothermal database for the Callisto experimental vehicle in the configuration with deployed landing legs. We described the numerical method used for the simulations and some of the post processing which is applied. We used the results to illustrate the influences of different trajectory and operation parameters on the aerothermal loads on the vehicle, with a focus on the landing legs. We showed, that the reverse flight with a retro-burn of the engine is a complex problem, which can necessitate a large number of simulations or experiments to successfully quantify critical thermal loads. The analyses of the influence of angle of attack and angle of roll demonstrated that even minor changes in attitude can have a relevant influence on the position of maxima and even on the question whether some surfaces change from being heated to being cooled. The investigation into the influence of Mach number and thrust level showed, that Ma has a bigger influence on the aerothermal loads, but that a lower Th can actually cause higher heat flux maxima for the same Ma and can therefore not be neglected. The study of different turbulence models illustrates that this modelling parameter has a big influence on the heat loads and on the flow field in general. We, therefore, highly recomend experimental validation of the numerical modelling. As in Callisto we were not able to obtain experimental data prior to the test flights, we instead opted to use the results to provide uncertainties for the ATD. We look forward to the Callisto test flight and hope to provide better information on this question after our post flight analysis.

5. Acknowledgments

The authors would like to thank all the colleagues from DLR, CNES and JAXA for their collaboration on this project, with special thanks going to the DLR ALS team and the CNES aero-science team.

References

[1] J.-P. Préaud, S. Dussy, J. B. Breteau, and J. B. Bru. “Preparing the Future of European Space Transportation: Reusable Technologies and Demonstrators”. In: *8th European Conference for Aeronautics and Space Sciences (EUCASS), Madrid, Spain*. July 2019. DOI: 10.13009/EUCASS2019-973.

[2] E. Dumont, S. Ishimoto, P. Tatiossian, J. Klevanski, B. Reimann, T. Ecker, L. Witte, J. Riehmer, M. Sagliano, S. G. Vincenzino, I. Petkov, W. Rotärmel, R. Schwarz, D. Seelbinder, M. Markgraf, J. Sommer, D. Pfau, and H. Martens. “CALLISTO: a Demonstrator for Reusable Launcher Key Technologies”. In: *32nd International Symposium on Space Technology and Science (ISTS)*. Fukui, Japan, June 2019.

[3] S. Krummen, J. Desmariaux, Y. Saito, M. Boldt, L. E. Briese, N. Cesco, C. Chavagnac, E. Cliquet-Moreno, E. Dumont, T. Ecker, S. Eichel, M. Ertl, S. Giagkozoglou, T. Glaser, C. Grimm, M. Illig, S. Ishimoto, J. Klevanski, N. Lidon, O. Mierheim, J.-F. Niccolai, S. Reershemius, B. Reimann, J. Riehmer, M. Sagliano, H. Scheufler, A. Schneider, S. Schröder, R. Schwarz, D. Seelbinder, M. Stief, J. Windelberg, and S. Woicke. “Towards a Reusable First Stage Demonstrator: CALLISTO - Technical Progresses & Challenges”. In: *72th International Astronautical Congress (IAC)*. IAC-21-D2.6.1. Oct. 2021. URL: https://elib.dlr.de/147143/.

[4] S. G. Vincenzino, W. Rotärmel, I. Petkov, H. Elsäßer, E. Dumont, L. Witte, and S. Schröder. “Reusable Structures for CALLISTO”. In: *8th European Conference for Aeronautics and Space Sciences (EUCASS)*. July 2019. URL: https://elib.dlr.de/129444/.

[5] L. Blackmore. “Frontiers of Engineering: Reports on Leading-Edge Engineering from the 2016 Symposium”. In: Washington, DC: The National Academies Press, 2017. Chap. Autonomous Precision Landingof Space Rockets, pp. 33–41. ISBN: 978-0-309-45036-2. DOI: 10.17226/23659. URL: https://nap.nationalacademies.org/catalog/23659/frontiers-of-engineering-reports-on-leading-edge-engineering-from-the.

[6] S. G. Vincenzino, S. Eichel, W. Rotärmel, F. Krziwanie, I. Petkov, E. Dumont, A. Schneider, S. Schröder, J. Windelberg, T. Ecker, and M. Ertl. “Development of Reusable Structures and Mechanisms for CALLISTO”. In: *33rd ISTS*. Feb. 2022. URL: https://elib.dlr.de/185598/.

[7] T. Ecker, S. Karl, E. Dumont, S. Stappert, and D. Krause. “Numerical Study on the Thermal Loads During a Supersonic Rocket Retropropulsion Maneuver”. In: *Journal of Spacecraft and Rockets* 57.1 (Jan. 2020), pp. 1–16. DOI: 10.2514/1.A34486.

[8] E. Dumont, T. Ecker, C. Chavagnac, L. Witte, J. Windelberg, J. Klevanski, and S. Giagkozoglou. "CALLISTO - Reusable VTVL launcher first stage demonstrator". In: *Space Propulsion Conference 2018*. Seville, Spain, May 2018. URL: https://elib.dlr.de/119728/.

[9] M. Laureti and S. Karl. "Aerothermal databases and load predictions for Retro Propulsion-Assisted Launch Vehicles (RETALT)". In: *CEAS Space Journal* (2022). ISSN: 1868-2510. DOI: 10.1007/s12567-021-00413-0. URL: https://doi.org/10.1007/s12567-021-00413-0.

[10] T. Ecker, M. Ertl, J. Klevanski, E. Dumont, and S. Krummen. "Aerothermal characterization of the CALLISTO vehicle during descent". In: *9th European Conference for Aeronautics and Space Sciences*. 2022.

[11] J. Riehmer, K. Kapteijn, J. Klevanski, B. Reimann, A. Gülhan, and E. Dumont. "Wind Tunnel Experiments of the CALLISTO VTVL Launcher in the TMK and HST Wind Tunnels". In: *9th European Conference for Aeronautics and Space Sciences*. 2022.

[12] J. Klevanski, E. Dumont, T. Ecker, M. Ertl, S. Krummen, B. Reimann, and J. Riehmer. "Progress in Aerodynamic Studies for CALLISTO - Reusable VTVL Launcher First Stage Demonstrator". In: *9th European Conference for Aeronautics and Space Sciences*. 2022.

[13] K. Hanemann, J. M. Schramm, A. Wagner, S. Karl, and V. Hanemann. *A Closely Coupled Experimental and Numerical Approach for Hypersonic and High Enthalpy Flow Investigations Utilising the HEG Shock Tunnel and the DLR TAU Code*. Tech. rep. DLR, 2010.

[14] Y. Wada and M.-S. Liou. "A flux splitting scheme with high-resolution and robustness for discontinuities". In: *32nd Aerospace Sciences Meeting and Exhibit*. 1994. DOI: 10.2514/6.1994-83.

[15] B. Thornber, A. Mosedale, D. Drikakis, D. Youngs, and R. Williams. "An improved reconstruction method for compressible flows with low Mach number features". In: *Journal of Computational Physics* 227.10 (2008), pp. 4873–4894. ISSN: 0021-9991. DOI: https://doi.org/10.1016/j.jcp.2008.01.036. URL: https://www.sciencedirect.com/science/article/pii/S0021999108000429.

[16] P. Spalart and S. Allmaras. "A one-equation turbulence model for aerodynamic flows". In: *30th Aerospace Sciences Meeting and Exhibit*. 1994. DOI: 10.2514/6.1992-439. eprint: https://arc.aiaa.org/doi/pdf/10.2514/6.1992-439. URL: https://arc.aiaa.org/doi/abs/10.2514/6.1992-439.

[17] D. C. Wilcox. "Reassessment of the scale-determining equation for advanced turbulence models". In: *AIAA Journal* 26.11 (1988), pp. 1299–1310. DOI: 10.2514/3.10041. eprint: https://doi.org/10.2514/3.10041. URL: https://doi.org/10.2514/3.10041.

[18] F. R. Menter, M. Kuntz, and R. Langtry. "Turbulence, Heat and Mass Transfer". In: ed. by K. Hanjalic, Y. Nagano, and M. J. Tummers. Begell House, 2003. Chap. Ten Years of Industrial Experience with the SST Turbulence Model.

[19] R.-D. Cécora, R. Radespiel, B. Eisfeld, and A. Probst. "Differential Reynolds-Stress Modeling for Aeronautics". In: *AIAA Journal* 53.3 (2015), pp. 739–755. DOI: 10.2514/1.J053250. eprint: https://doi.org/10.2514/1.J053250. URL: https://doi.org/10.2514/1.J053250.